
Compensation for Three-Dimensional Detector Response, Attenuation and Scatter in SPECT Grey Matter Imaging Using an Iterative Reconstruction Algorithm Which Incorporates a High-Resolution Anatomical Image

Hee-Joung Kim, Barry R. Zeeberg, and Richard C. Reba

Department of Radiology, George Washington University, Washington, DC

The use of SPECT to diagnose physiological alterations in disease states depends on the potential of SPECT to provide a quantitatively accurate reconstructed image. However, the reconstructed values depend upon the shape and size of the brain region as strongly as they depend upon true radioactivity concentration. We report here the results of applying an iterative reconstruction algorithm (IRA) to compensate for shape- and size-dependence, as well as for attenuation and scatter. The IRA is designed only for the reconstruction of images for which the true radioactivity in the white matter within the actual brain is negligible compared with the true radioactivity in the grey matter within the actual brain. The IRA incorporates an accurate three-dimensional model of detector response and utilizes an MRI image which defines the anatomical features of the brain being imaged by segmenting the grey, white and ventricular regions. It is the assumption of radioactivity localization exclusively in the grey matter which permits the efficient incorporation of the MRI image. The IRA was validated by simulation studies that utilized a slice through the basal ganglia in the realistic Hoffman three-dimensional mathematical brain model. FBP images deviate significantly from true radioactivity distribution, whereas IRA images are nearly identical to true radioactivity distribution, except for random fluctuations due to the presence of statistical noise. These results indicate that the application of the IRA will permit SPECT to distinguish deficits due to true physiological changes from apparent deficits due to imaging/reconstruction artifacts.

J Nucl Med 1992; 33:1225-1234

With the use of the muscarinic acetylcholinergic receptor binding radioligand (R,R)-[¹²³I]4IQNB and a triple-headed SPECT system with ultra high-resolution (UHR)

Received Oct. 3, 1991; revision accepted Feb. 26, 1992.
For reprints contact: Barry Zeeberg, PhD, Department of Radiology, Radio-pharmaceutical Chemistry, Room 662 Ross Hall, 2300 I St. NW, Washington, DC 20037.

parallel-hole collimators, we have found apparent deficits in the posterior parietal cortex (1). These apparent deficits may be due to altered radioactivity localization or to imaging/reconstruction artifacts. Interpretation of such an image and diagnosis of a disease state will require determining whether the apparent cortical variability is due to an underlying physiological cause or due to imaging/reconstruction artifacts.

The quantitative potential of SPECT or PET for estimating regional concentration of radioactivity is degraded by inaccuracies in image reconstruction. In particular, a shape- and size-dependent recovery coefficient, partial volume effects, resolution nonuniformity and scatter (2,3) will, in many instances, cause two regions with identical radioactivity concentration to appear to have significantly different radioactivity concentrations in the reconstructed image. Simulation studies (4,5) have shown that for a uniform true distribution of radioactivity in grey matter, there are apparent regional differences of radioligand localization caused by variation in the effective regional thickness of cortical grey matter. This variation is the result of different amounts of cortical infolding along the circumference of the cortex. For example, the infolding is greater at the frontal and occipital regions.

These apparent differences arise from the facts that: (a) there is finite detector resolution and sampling and (b) an incorrect reconstruction algorithm has been applied—that is, the assumptions underlying the application of the filtered backprojection (FBP) reconstruction algorithm are not strictly valid. In order to compensate for items a and b, we have developed an algorithm for the reconstruction of grey matter images which incorporates both a realistic model of the data collection process and the anatomical information available in the high-resolution MRI image.

METHODS

Three-Dimensional Computer Simulation Procedure

The mathematical three-dimensional Hoffman brain model (6) has a transaxial resolution of 1 mm and an axial spacing of 6

mm. In order to represent the three-dimensional brain model at a voxel resolution of $3 \text{ mm} \times 3 \text{ mm} \times 3 \text{ mm}$, we sampled every third voxel within the transaxial slice, and then duplicated and extended each transaxial slice to an axial length of 2 voxels.

The simulated projection data are built up as the successive summation of projection data for each nonzero voxel (4,5). For each nonzero voxel, the three-dimensional model of detector response (measured using the Trionix Triad SPECT system with UHR parallel-hole collimators) is multiplied by the voxel value, translated according to the voxel position and summed into an array containing the accumulated simulated projection data. Symbolically, a nonzero voxel at position (i,j,k) contributes $\text{OBJ}(i,j,k)3\text{-DPSF}(i'-i,j'-j,k'-k)$ to $\text{PROJ}(i',j',k')$, where PROJ is the simulated projection data and OBJ is the mathematical radioactive object. This computation is object-driven. We used an analytical expression for the 3-DPSF which explicitly included the distance- and depth-dependence of the amplitude A and the standard deviation σ (5).

When attenuation was included in the simulation, the method for simulating the projection data was modified by multiplying the voxel value by an attenuation factor. The attenuation factor was computed using a constant attenuation coefficient equal to 0.15 cm^{-1} and an attenuation path length equal to the distance between the voxel and the boundary of the attenuating medium, along a line perpendicular to the detector face. When attenuation was included in the simulation, the FBP reconstructed image was corrected for the attenuation effects with Chang's first-order method (7) using an effective attenuation coefficient equal to 0.12 cm^{-1} because of the presence of scatter in all of the simulations in which we included attenuation (8,9).

Scatter was represented as the sum of two Gaussian components (5). When scatter was included in the simulation, three separate simulations were performed, one for the detector response and two for the scatter, and the projection data from each of the three simulations were added together prior to the addition of noise or reconstruction (5). When noise was included in the simulation, the projection data were scaled to the desired number of acquired counts, and Poisson noise was computed using the rejection method (5,10).

Brain Models

Based upon the mathematical brain model of Hoffman et al. (6), we utilized three different "true" distributions of radioactivity: (a) a uniform cortical grey matter radioactivity distribution (Fig. 1A), (b) a 30% right parietal cortical deficit (Fig. 1B) and (c) a "sinusoidal" brain model (Fig. 1C), in which the radioactivity in the grey matter voxels was set equal to $1 + A \sin(Bx+C)\sin(Dy+E)$ for the voxel at location (x, y) . We selected $A = 0.3$, $B = D = 0.28 \text{ rad voxel}^{-1}$ and $C = E = 0 \text{ voxel}^{-1}$. A circumferential path through the cortical grey matter (Fig. 1D) was used for determining which voxels would be included in the circumferential profiles (see Data Analysis).

FBP

The projection data were reconstructed as previously described (4,5). FBP using a Hamming filter with cutoff frequency 0.12 mm^{-1} (0.36 pixel^{-1}) was utilized for reconstruction.

IRA

The IRA was applied to an image in which the radioactivity distribution is restricted to the grey matter. The data sets required for the IRA are shown in Figure 2. The "true" radioactivity

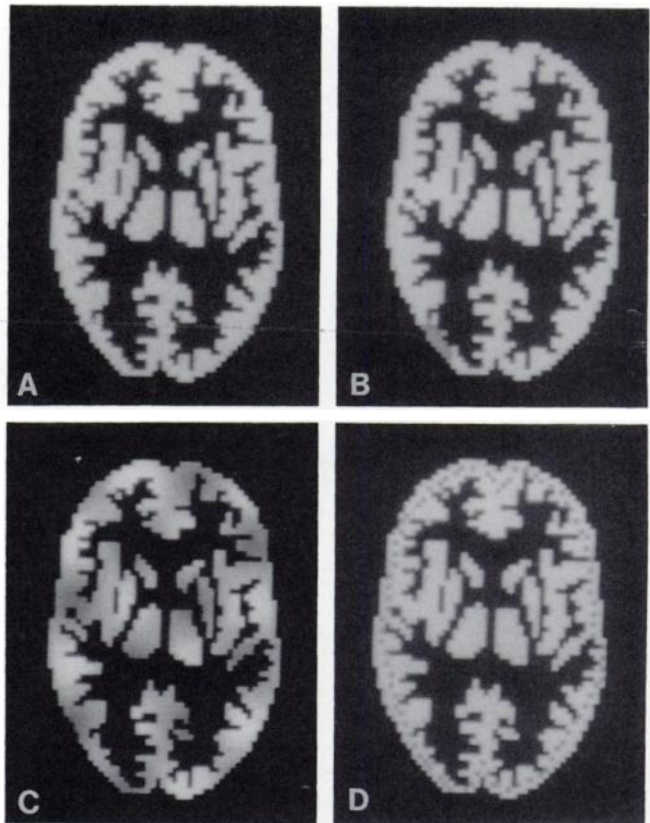


FIGURE 1. Digitized transverse slice at the level of the basal ganglia chosen from the three-dimensional Hoffman brain model (6) indicating uniform distribution of radioactivity throughout the grey matter (A), right parietal cortical deficit brain model (B), sinusoidal brain model (C), and circumferential path through the cortical grey matter (D). For display purposes, each brain image was normalized to its own maximum.

distribution resulted in a set of "measured" projection data, which were computed using the three-dimensional simulation procedure (5). For simulations with noise, the projection data were scaled to a desired level of acquired counts, and Poisson noise was added to the scaled projection data. Poisson noise was computed using the rejection method (10). The measured projection data corresponded to physically observable projection data and were subsequently reconstructed using FBP. When FBP was used as an internal part of the IRA, no attenuation correction was applied.

Grey matter voxels in the corresponding grey matter voxel ("GMV") image [grey matter voxels in the MRI image were defined as the grey matter voxels in the Hoffman brain model (6)] were set to an initial estimate. For example, all grey matter voxels may be set equal to a constant and, throughout the entire IRA process, all nongrey matter voxels were set to 0. The projection data arising from GMV radioactivity distribution defined by this initial guess were computed using the three-dimensional simulation procedure. When this simulation included attenuation and/or scatter, then simulation of the projection data within the IRA also included attenuation and/or scatter. Attenuation and/or scatter were thus implicitly included within the IRA, which therefore directly compensated for these degrading factors without any additional correction factors, such as the Chang attenuation correction algorithm (7).

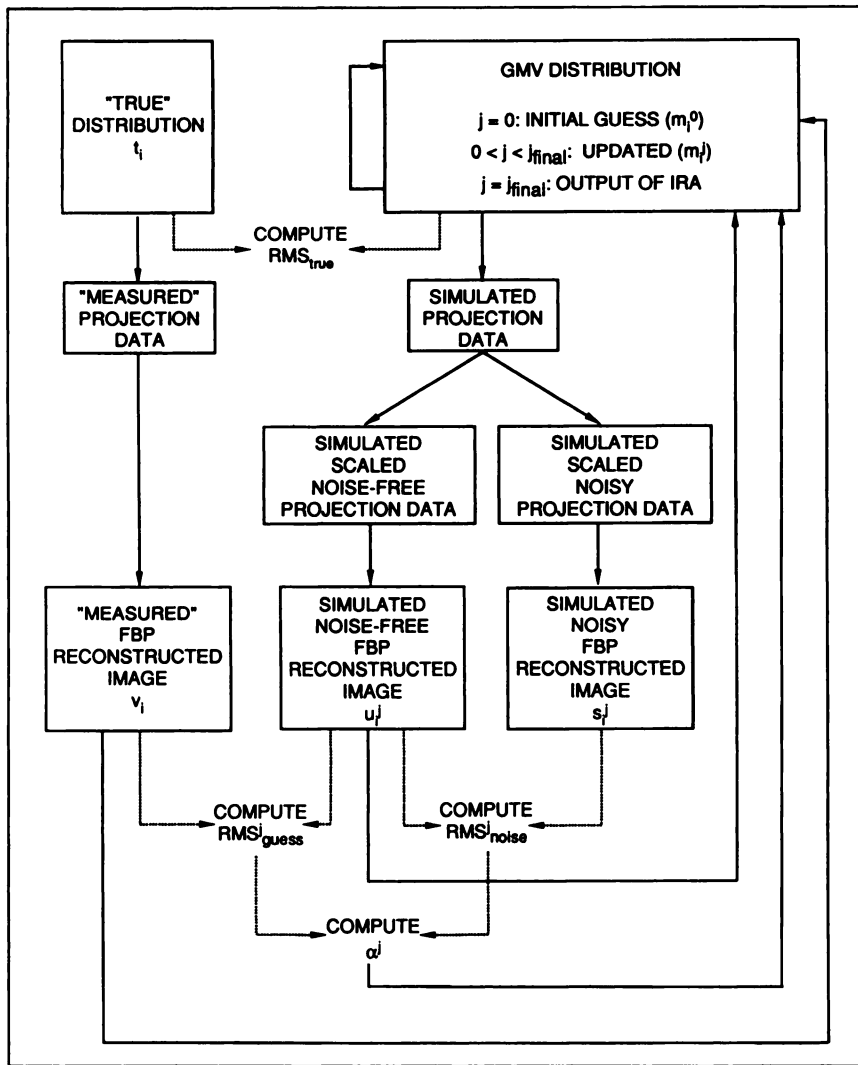


FIGURE 2. Flow diagram of the implementation of the IRA. Data sets are enclosed within rectangular boxes. Solid arrows represent the relationship of the data sets. Dotted arrows represent computations.

The IRA may be summarized as follows: At each iteration, each of the grey matter voxels (as defined by GMV distribution) within the FBP reconstruction from the measured projection data was compared with the corresponding voxel within the FBP reconstruction from the noiseless simulated projection data (see Fig. 2), and from these values the corresponding voxel within the GMV distribution was updated using Equation 4 below. A new set of noiseless projections (as well as a set of projections with noise) was formed from the GMV distribution with the three-dimensional computer simulation procedure, and from this a new reconstruction was generated by the FBP, representing the updated reconstruction from the simulated projection data. This procedure was repeated through multiple iterations. The final GMV distribution was considered to represent the reconstruction of the true distribution.

The root-mean-square (RMS) error in the reconstructed image due to the added Poisson noise was computed as

$$RMS_{noise} = \{\sum_{i(i \in grey\ matter)} (s_i - u_i)^2 / n\}^{.5}, \quad \text{Eq. 1}$$

where s_i and u_i represent the i^{th} voxels in the FBP reconstructed image derived from the noisy and from the noise-free simulated projection data, respectively, and n is the number of grey matter

voxels. The RMS error in the reconstructed image due to both Poisson noise and deviations of the initial guess from the true radioactivity distribution was computed as

$$RMS_{guess} = \{\sum_{i(i \in grey\ matter)} (u_i - v_i)^2 / n\}^{.5}, \quad \text{Eq. 2}$$

where v_i represents the i^{th} grey matter voxel in the FBP reconstructed images derived from the true radioactivity distribution.

A relaxation factor, α , was computed as

$$\alpha = (1 - RMS_{noise} / RMS_{guess}) / 2, \quad \text{Eq. 3}$$

The purpose of α is to prevent the iteration from reducing RMS_{guess} below RMS_{noise} , the Poisson noise in the reconstructed image (for noiseless simulations, $\alpha = 0.5$). For the i^{th} grey matter voxel m_i within the GMV image, the current guess (for the j^{th} iteration) of the radioactivity value, m_i^j , was upgraded by the formula

$$m_i^{j+1} = m_i^j [(v_i / u_i^j - 1) \alpha^j + 1], \quad \text{Eq. 4}$$

where the superscripts are not exponents but are the iteration numbers. The values of RMS_{guess}^{j+1} and RMS_{noise}^{j+1} were recalculated

at each iteration as

$$\text{RMS}_{\text{noise}}^{j+1} = \{\sum_{i(\text{grey matter})} (s_i^{j+1} - u_i^{j+1})^2 / n\}^{.5} \quad \text{Eq. 5}$$

$$\text{RMS}_{\text{guess}}^{j+1} = \{\sum_{i(\text{grey matter})} (u_i^{j+1} - v_i)^2 / n\}^{.5} \quad \text{Eq. 6}$$

and the value of α^{j+1} was recalculated at each iteration as

$$\alpha^{j+1} = (1 - \text{RMS}_{\text{noise}}^{j+1} / \text{RMS}_{\text{guess}}^{j+1}) / 2. \quad \text{Eq. 7}$$

In our initial studies, we found that each iteration reduced the difference ($\text{RMS}_{\text{guess}}^{j+1} - \text{RMS}_{\text{noise}}^{j+1}$) to approximately one-half of the previous difference ($\text{RMS}_{\text{guess}}^j - \text{RMS}_{\text{noise}}^j$). Since our goal was to stop when $\text{RMS}_{\text{guess}}^{j+1} \approx \text{RMS}_{\text{noise}}^{j+1}$, we performed approximately 10 iterations, which reduced the difference ($\text{RMS}_{\text{guess}}^{10} - \text{RMS}_{\text{noise}}^{10}$) to approximately 0.1% of the difference ($\text{RMS}_{\text{guess}}^0 - \text{RMS}_{\text{noise}}^0$). The output of the IRA is the final updated GMV distribution defined as in Equation 4.

The IRA is based upon the idea that both the projection and reconstruction processes are linear, so that for the i^{th} grey matter voxel the ratio of its radioactivity values in the GMV guess/true radioactivity distribution $\approx u_i/v_i$. That is, the ratio in the FBP reconstructed image space is an approximation of the ratio in the original object space. With other iterative approaches (such as maximum likelihood or ART), the residual errors in the projection data are used to correct the estimate of the true radioactivity distribution. In comparison, the advantage of using the IRA is that residual errors are localized to a specific voxel in the image rather than distributed along the large number of image voxels which contribute to a given voxel in the projection data. However, because of the existence of noise, we cannot apply the entire amount of correction, but rather require a damping factor α .

In some studies, we applied the IRA to an isolated slice, and in other studies we applied the IRA to a slice within the full three-dimensional brain model. In the latter case, a simplification was required because of the excessive computational time required using our microcomputer: The true distribution of radioactivity within the grey matter of all the slices other than the selected slice was uniform; only the selected slice had an unknown radioactivity distribution to be reconstructed. The true radioactivity distribution within the selected slice was either the right parietal cortical deficit model (Fig. 1B) or the sinusoidal model (Fig. 1C). In the three-dimensional simulations, we utilized a 9-mm thickness for the selected slice and scaled the projection data for this slice (equal to the sum of the projection data originating within the slice plus the projection data originating from within neighboring slices) to 2.0×10^6 counts prior to the addition of Poisson noise. The simulation also included attenuation and scatter effects.

Because of the three-dimensional detector response and scatter, some of the counts originating from the neighboring slices will be detected within the projection data for the selected slice. Approximately 52.4% of the counts within the projection data for the selected slice had originated as nonscattered counts from within the projection data for the selected slice had originated as nonscattered counts from within the selected slice; the remainder of the counts arose from the convolution of radioactivity outside of the selected slice with the three-dimensional detector response function (17%), or from scatter originating within (2.6%) or outside (28%) the selected slice. Because preliminary results indicated convergence by approximately the fourth iteration when we applied the IRA to a slice within the full three-dimensional

brain model in the presence of noise, we stopped the IRA after the fourth iteration.

Data Analysis

Circumferential cortical profiles were determined as described previously (4,5,11) using the circumferential path drawn on the theoretical map of grey matter. Data obtained using circumferential profiles were normalized such that their means were equal to unity.

Scatter plots of the relative % errors were obtained by normalizing the FBP and IRA reconstructed images and the true radioactivity distribution to a mean of unity prior to subtraction of the true radioactivity distribution from the reconstructed images.

Convergence of the IRA was examined for the sinusoidal model either as an isolated single slice in the absence of attenuation and scatter, or as a slice embedded within a three-dimensional brain in the presence of three-dimensional detector response, attenuation, scatter and noise. The true radioactivity distribution and the GMV guess at each iteration were individually normalized to a mean of unity. The value in each grey matter voxel of the normalized true radioactivity distribution was then subtracted from the corresponding voxel of the normalized GMV guess and the RMS error, RMS_{true} , computed from these differences:

$$\text{RMS}_{\text{true}}^i = \{\sum_{i(\text{grey matter})} (m_i^j - t_i)^2 / n\}^{.5}, \quad \text{Eq. 8}$$

where t_i represents the i^{th} voxel in the true image. Before subtraction, m_i^j and t_i are first normalized so that the means over all grey matter voxels are equal to unity.

RESULTS

Isolated Two-Dimensional Brain Slice

To demonstrate the convergence properties of the IRA, we have computed two different measures of the error in the current IRA estimate of true radioactivity distribution: $\text{RMS}_{\text{guess}}$ (Equation 6) and RMS_{true} (Equation 8). RMS_{true} cannot be determined in a real imaging situation, since the true radioactivity distribution would need to be known; thus $\text{RMS}_{\text{guess}}$ must be used as an approximation to RMS_{true} . For an isolated sinusoidal brain slice, RMS_{true} has converged by the ninth iteration (Fig. 3). Thus, we chose to terminate the IRA at the ninth iteration for isolated two-dimensional brain slices. The value of α (Fig. 3) tends to decrease with increasing iteration numbers. $\text{RMS}_{\text{noise}}$ (Equation 5) is essentially independent of iteration number (not shown).

To demonstrate the quantitative accuracy of the IRA, we reconstructed noise-free simulated projection data for a uniform cortical grey matter radioactivity distribution (Fig. 1A) and for a right parietal cortical deficit model (Fig. 1B), using FBP (Fig. 4A) or IRA (Fig. 4B) (not shown for the uniform model). FBP of both models resulted in circumferential cortical profiles that exhibited 2- to 3-fold cortical variations (Fig. 4C), although (except for the deficit in the right parietal cortex deficit model) these profiles should theoretically be constant. The deficit in the deficit model is discernible when a comparison is made against the uniform model (Fig. 4C). In practice, however, the

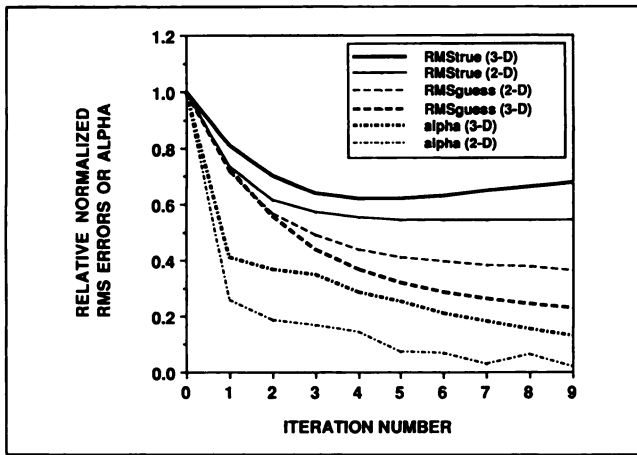


FIGURE 3. Convergence of the IRA applied to an isolated brain slice or a brain slice embedded within the three-dimensional brain for the sinusoidal brain model.

reconstructed image resulting from the exactly matching uniform model will not be available for this comparison, and the trough due to the deficit will not be distinguishable from normally-occurring troughs due to normal variations in effective cortical thickness. In contrast, for the IRA, the circumferential profiles for both the uniform and deficit models were constant, except for the expected 30% deficit in right parietal cortex for the deficit model (Fig. 4D). These results show that IRA can compensate for variations due to imaging artifacts to permit the quantitation of physiological variations.

The simulated projection data for the deficit model were scaled to a total of 500,000 counts/slice, and Poisson noise was added to the scaled projection data. The noisy projection data were reconstructed using IRA (Fig. 4E). A comparison of the circumferential profiles of the noisy IRA reconstructed image and the theoretical image (Fig. 4D)

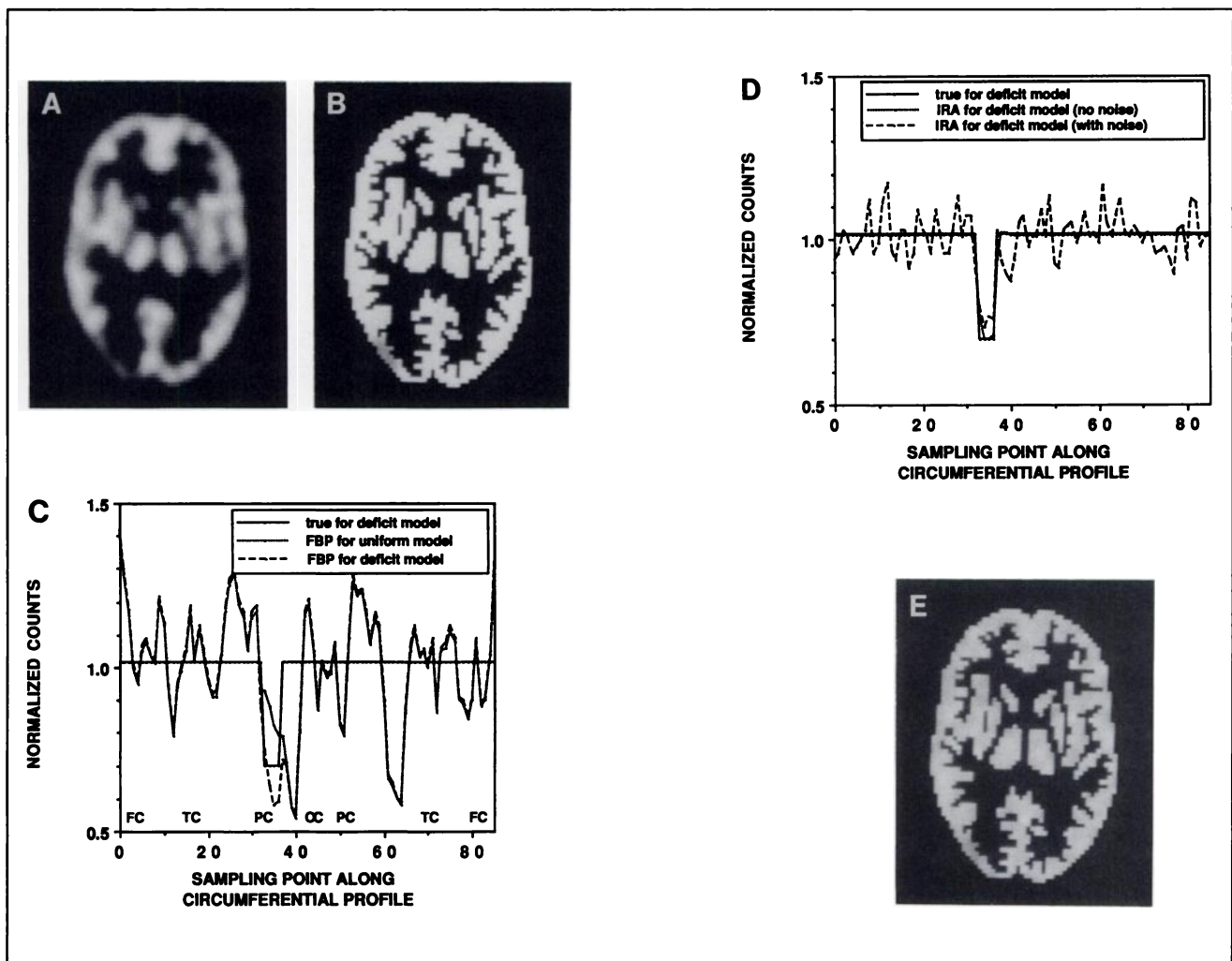


FIGURE 4. Noise-free FBP reconstructed image (A) and noise-free IRA reconstructed image (B) for the right parietal cortical deficit model, circumferential profiles for FBP for the uniform and right parietal cortical deficit models (C), circumferential profiles for IRA (D) and noisy IRA reconstructed image (E). In (C), because of the large degree of agreement, it is difficult to distinguish the circumferential profiles for the FBP from the uniform and deficit models, except in the region of the deficit. In (D), because of the large degree of agreement, it is difficult to distinguish the noise-free IRA and the theoretical circumferential profiles. In (C), FC, TC, PC, OC denote frontal cortex, temporal cortex, parietal cortex and occipital cortex, respectively.

indicates the accuracy of the IRA even in the presence of a realistic level of statistical noise.

The brain model containing a single deficit is rather oversimplified. We therefore simulated a sinusoidal brain model (Fig. 1C) in the absence of noise, using both FBP (Fig. 5A) and IRA (Fig. 5B). Deviations in the FBP reconstructed image can be demonstrated quantitatively by comparison of the circumferential profile with the theoretical circumferential profile (Fig. 5C). The accuracy of the IRA reconstructed image can be demonstrated quantitatively by comparison of the circumferential profile with the theoretical circumferential profile (Fig. 5D).

The simulated projection data for the sinusoidal model were scaled to a total of 500,000 counts/slice, and Poisson noise was added to the scaled projection data. The noisy projection data were reconstructed using IRA (Fig. 5E). A comparison of the circumferential profiles of the noisy IRA reconstructed image and the theoretical image (Fig.

5D) indicates the accuracy of the IRA even in the presence of a realistic level of statistical noise.

Brain Slice Within a Three-Dimensional Brain Model

For the brain slice embedded within a three-dimensional brain, RMS_{true} had converged by the fourth iteration (Fig. 3). Thus, we chose to terminate the IRA at the fourth iteration for brain slices embedded within a three-dimensional brain. The value of α (Fig. 3) tends to decrease with increasing iteration numbers. RMS_{noise} (Equation 5) is essentially independent of an iteration number (not shown).

A comparison of the noise-free attenuation-corrected FBP (Fig. 6A) and the IRA (Fig. 6B) reconstructed images for the right parietal cortical deficit model indicates the superiority of the IRA. Circumferential profiles (Fig. 6C) quantitatively indicate the superiority of the IRA. Similarly, a comparison of the noise-free attenuation-corrected

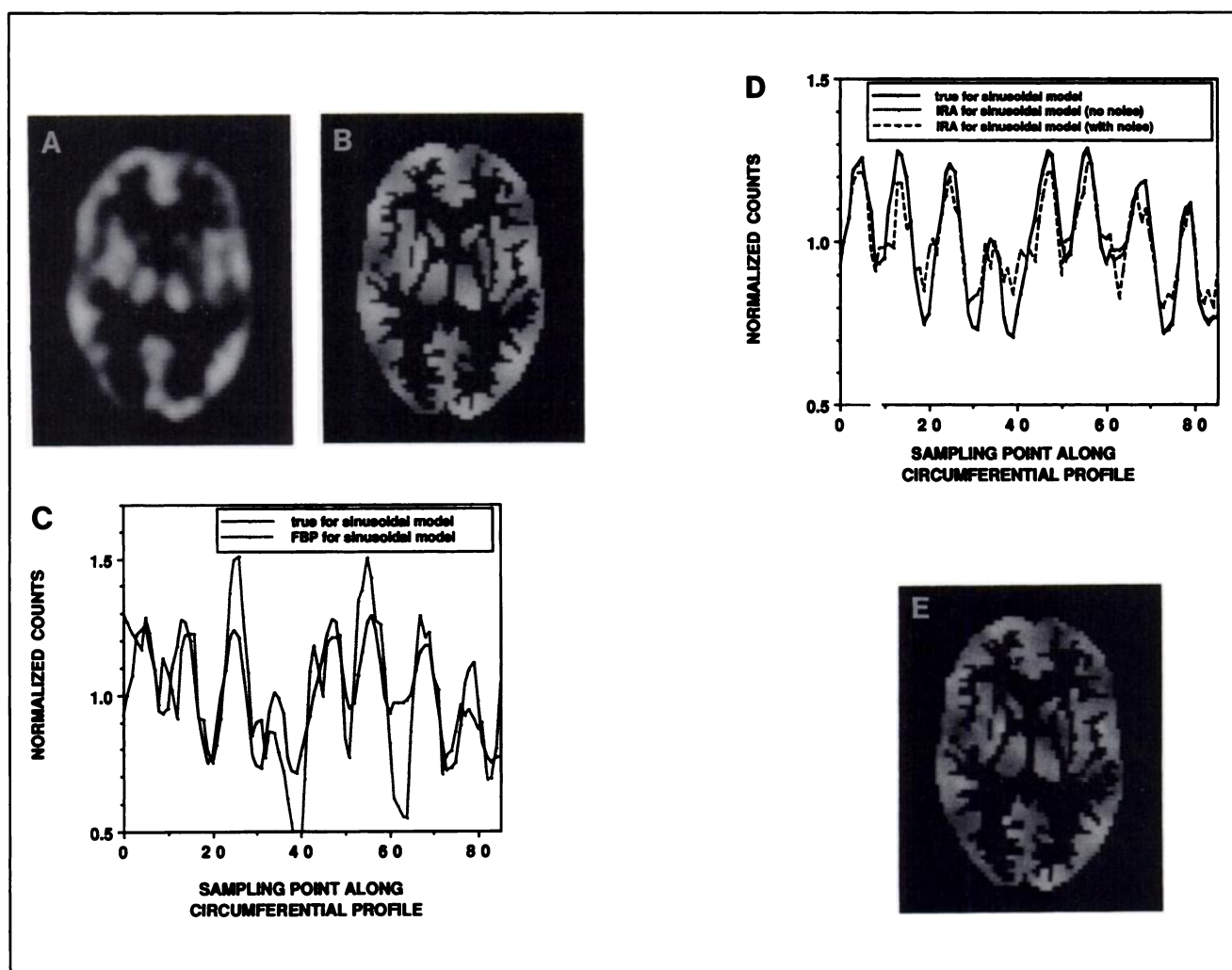


FIGURE 5. Noise-free FBP reconstructed image (A) and noise-free IRA reconstructed image (B) for the sinusoidal brain model, circumferential profiles for FBP (C), circumferential profiles for IRA (D) and noisy IRA reconstructed image (E). In (D), because of the large degree of agreement, it is difficult to distinguish the noise-free IRA and the theoretical circumferential profiles.

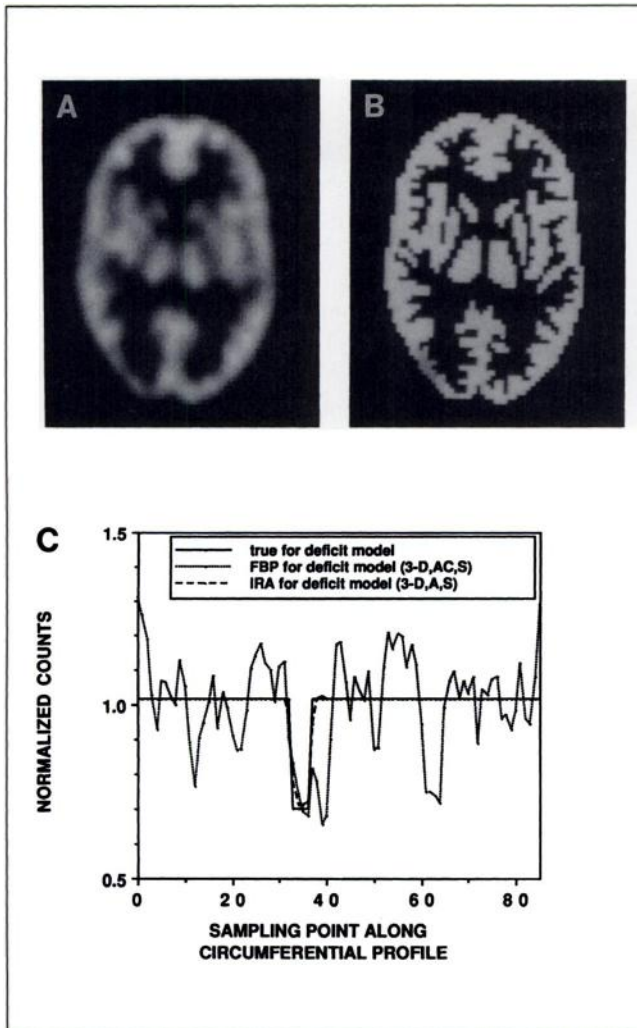


FIGURE 6. Noise-free FBP reconstructed image (A) and noise-free IRA reconstructed image (B) for the right parietal cortical deficit model in the presence of an out-of-slice contribution ("3-D"), attenuation ("A"), and scatter ("S") in the projection data, and circumferential profiles for the true image, FBP and IRA (C). The FBP image was corrected for attenuation ("AC") using the Chang method (7) with an attenuation coefficient of 0.12/cm (8,9). In (C), because of the degree of agreement, it is difficult to distinguish the noise-free IRA and the theoretical circumferential profiles.

FBP (Fig. 7A) and the IRA (Fig. 7B) reconstructed images for the sinusoidal as well as scatter plots (Figs. 7C-D) quantitatively indicate the superiority of the IRA.

A comparison of the noisy attenuation-corrected FBP (Fig. 8A) and the IRA (Fig. 8B) reconstructed images for the right parietal cortical deficit model indicates the superiority of the IRA. Circumferential profiles (Fig. 8C) quantitatively indicate the superiority of the IRA. Similarly, a comparison of the noisy attenuation-corrected FBP (Fig. 9A) and the IRA (Fig. 9B) reconstructed images for the sinusoidal model again indicates the superiority of the IRA. Scatter plots (Fig. 7C, 9C) again quantitatively indicate the superiority of the IRA.

Except for the region containing the deficit, the FBP

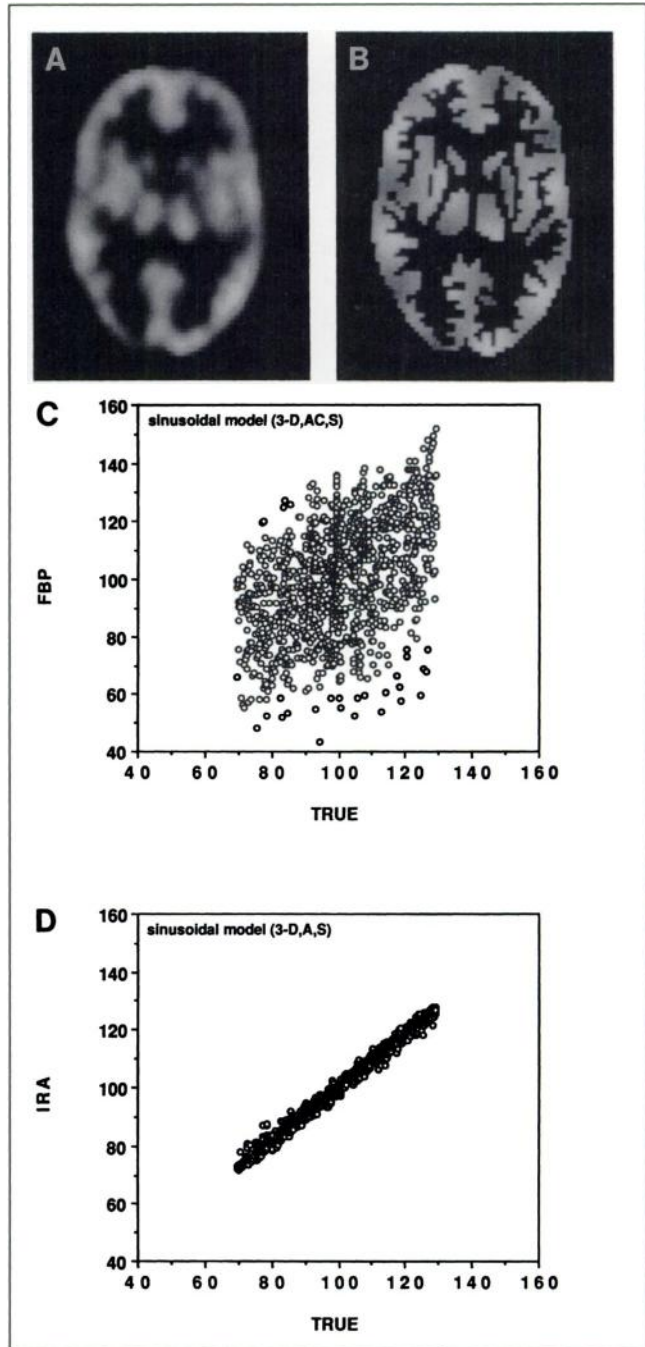


FIGURE 7. Noise-free FBP reconstructed image (A) and noise-free IRA reconstructed image (B) for the sinusoidal model in the presence of an out-of-slice contribution, attenuation and scatter in the projection data, and scatter plots for FBP (C) and IRA (D) versus the true image. The FBP image was corrected for attenuation using the Chang method (7) with an attenuation coefficient of 0.12/cm (8,9).

reconstructed values for the right parietal cortical deficit model in the absence of noise deviate significantly from the true values in a manner which reflects anatomical variations (compare Figs. 1D and 6C). A scatter plot of the relative % errors in 1,111 grey matter voxels (omitting the 20 voxels within the deficit region) in a noise-free FBP

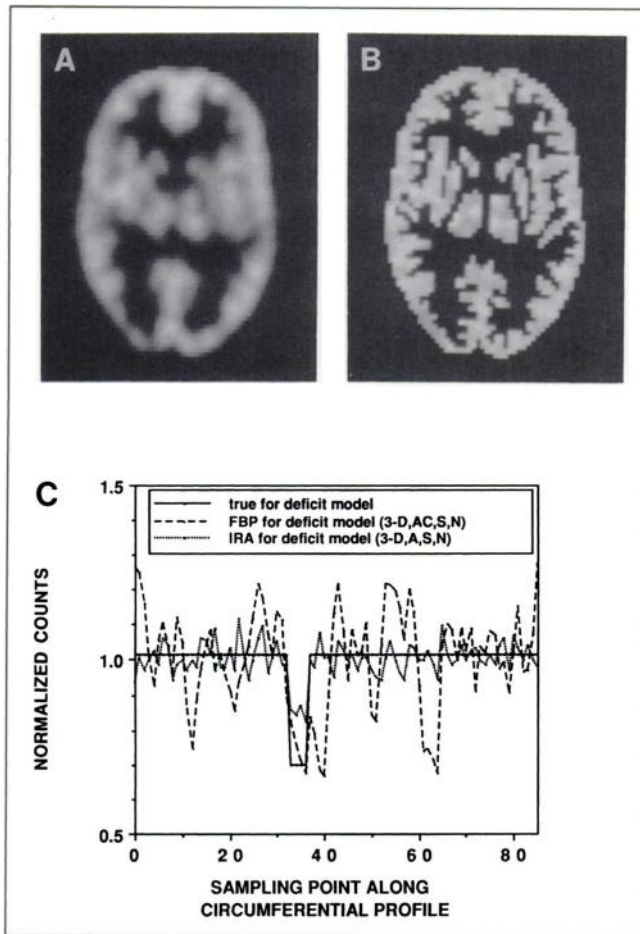


FIGURE 8. Noisy ("N") FBP reconstructed image (A) and noisy IRA reconstructed image (B) for the right parietal cortical deficit model in the presence of an out-of-slice contribution, attenuation and scatter in the projection data, and circumferential profiles for the true image, FBP and IRA (C). The FBP image was corrected for attenuation using the Chang method (7) with an attenuation coefficient of 0.12/cm (8,9).

reconstructed image (horizontal axis) and the relative % errors in a noisy IRA reconstructed image (vertical axis) for the right parietal cortical deficit model indicates that there is an insignificant dependence of the errors in the IRA image upon the errors in the FBP image (Fig. 10). Since the errors in the FBP image represent the effects of anatomical variation, the insignificant correlation ($r = 0.071$) indicates that the IRA has removed the effects of anatomical variation from the reconstructed image. The wider spread of the errors for FBP in the absence of noise (-50% to $+40\%$) than for the IRA in the presence of noise (-20% to $+20\%$) indicates the superior quantitative accuracy of the IRA.

noise is not shown, since it was nearly identical with that for FBP in the absence of noise (Fig. 7C). The FBP image was corrected for attenuation using the Chang method (7) with an attenuation coefficient of 0.12/cm (8,9).

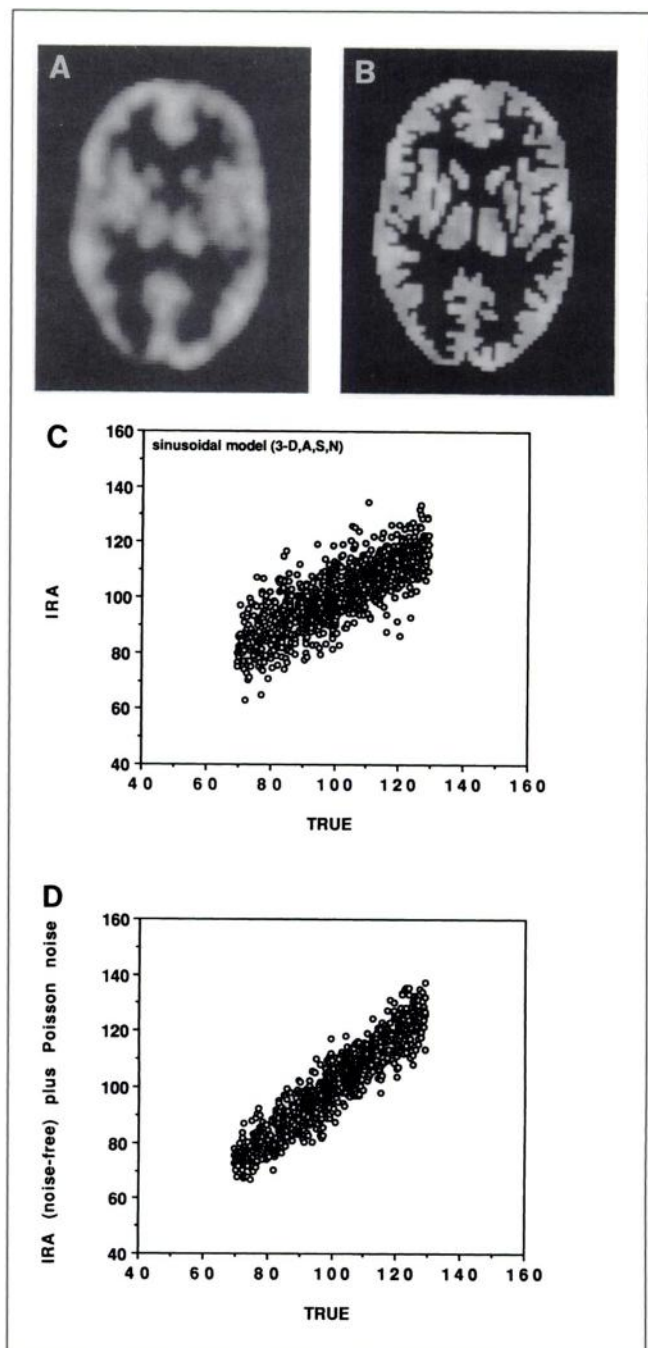


FIGURE 9. Noisy FBP reconstructed image (A) and noisy IRA reconstructed image (B) for the sinusoidal model in the presence of an out-of-slice contribution, attenuation and scatter in the projection data, scatter plot for IRA versus the true image (C) and scatter plot for noise-free IRA plus added Poisson noise (D). The scatter plot for (D) was computed to show that the broadening of the scatter plot in the presence of noise in comparison with the scatter plot in the absence of noise (Fig. 7D), which resulted primarily from the statistics of the noise rather than from a degradation of the accuracy of the IRA in the presence of noise. The noise was added to the noise-free IRA scatter plot using the rejection method (10) based upon the total counts in the projection data equal to 2×10^6 and the fact that 52% of the counts in the projection data were nonscattered counts originating from within the slice to be reconstructed and the "naive prediction" of Budinger et al. (12). The scatter plot for FBP in the presence of

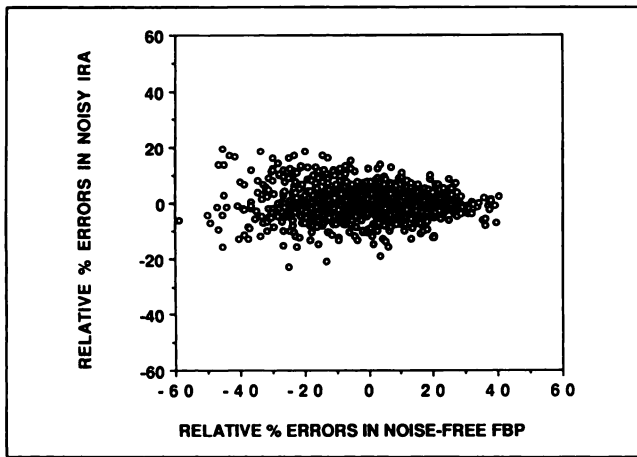


FIGURE 10. Scatter plot of the relative % errors in 1,111 grey matter voxels (omitting the 20 voxels within the deficit region) in a noise-free FBP reconstructed image in the absence of an out-of-slice contribution, attenuation, or scatter (horizontal axis) and the relative % errors in a noisy IRA reconstructed image with the same parameters (vertical axis) for the right parietal cortical deficit model. The errors in the FBP image represent the effects of anatomical variation, so that the insignificant correlation ($r = 0.071$) indicates that the IRA has removed the anatomical variation effects from the reconstructed image.

DISCUSSION

Cortical circumferential profiles demonstrate that FBP reconstructed images can exhibit significant quantitative deviations from the true radioactivity distribution for a uniform (Fig. 4C), deficit (Fig. 4C) and sinusoidal (Fig. 5C) model. In particular, the apparent deficits in the simulated reconstructed image of the uniform model (Fig. 4C) indicate that it may be difficult to interpret an apparent deficit in a physically measured human brain image as resulting from a true radioactivity deficit or from an imaging artifact. In order to compensate for these degradations, we have developed the IRA, which utilizes a realistic model of the data collection process.

The IRA is designed for the reconstruction only of grey matter images. These images must be acquired at a time when true radioactivity in the white matter within the actual brain is negligible compared with true radioactivity in the grey matter. The IRA incorporates an accurate model of the three-dimensional detector response and utilizes an MRI image which defines the anatomical features of the brain being imaged by segmenting the grey, white and ventricular regions. It is the assumption of radioactivity localization exclusively in the grey matter that permits the efficient incorporation of the MRI image.

For both the two- and three-dimensional models, in the presence or absence of attenuation, scatter and noise, the IRA reconstructed images are much closer to the true radioactivity distribution, and the ambiguity of interpreting a deficit as being real or artifactual is removed. Although the reconstructed IRA image will allow us to diagnose a deficit as arising from a true physiological

change, because of its random nature statistical noise cannot be compensated for by the IRA, and its presence prevents the IRA from providing a perfect compensation for finite detector response. Noise thus represents a fundamental limitation of our ability to determine the image in a quantitatively accurate manner.

These simulation studies and the IRA incorporated several unique features: (a) the application of realistic three-dimensional distance- (between the source of radioactivity and the detector) and depth- (between the source of radioactivity and the boundary of the scattering medium) dependent detector response function; (b) the application of the realistic Hoffman mathematical three-dimensional brain model; and (c) a high-resolution MRI anatomical image was used in order to compensate for artifacts due to anatomical variations.

Since we have not presented a rigorous mathematical proof of the convergence of the IRA, the method's validity is demonstrated by the empirical results presented in this paper. These results are sufficient to show that realistic grey matter radioactivity distribution can be accurately estimated using the IRA. In a recent paper (13), an alternate iterative reconstruction method was applied to realistic simulated projection data derived from the mathematical Hoffman brain model (6) in the absence of scatter and noise, and in the presence of attenuation and distance-dependent detector response. This method (three-dimensional maximum likelihood-EM) resulted in a % RMS error which was similar to that for FBP. Since we have shown here the superiority of IRA over FBP, we conclude that the IRA is also superior to three-dimensional maximum likelihood-EM. In a second recent paper (14), an EM algorithm was applied iteratively to measured three-dimensional Hoffman physical phantom projection data in the frequency domain, again utilizing a distance-dependent detector response. Quantitative results were not presented; however, the visual appearance of the reconstructed images was similar to that for FBP. We are not aware of other simulation studies using an iterative reconstruction method applied to a realistic brain model and a realistic detector response function. Three recent reports have appeared in which high-resolution anatomical information was incorporated during the reconstruction of emission tomographic images (15-17).

When the IRA is applied to a real brain image rather than to a simulated brain image, a high-resolution MRI anatomical image is needed in order to compensate for artifacts due to anatomical variations. The anatomical images will need to be segmented into grey matter regions and registered with the SPECT images. This study did not utilize an actual MRI image but assumed instead that the true shape of the grey matter distribution, as well as the exact nature of the detector response, attenuation and scatter were precisely known a priori. The simulated reconstructions presented here were therefore more accurate than could be achieved when imaging a real brain using

an experimentally acquired MRI image with imperfect segmentation and registration.

ACKNOWLEDGMENTS

The authors would like to thank Drs. Frank B. Atkins, Murray H. Loew and Frederic H. Fahey for useful discussions and suggestions. This work was supported by a grant from the National Institutes of Health (NS22215) and, in part, by a grant from the Department of Energy (DE FG05 88ER60649).

REFERENCES

1. Kim HJ. Quantitative accuracy of single photon emission computed tomography in neuroimaging by computer simulation. DSc dissertation, George Washington University. 1991.
2. Hoffman EJ, Huang SC, Phelps ME. Quantitation in positron emission computed tomography. 1. Effect of object size. *J Comput Assist Tomogr* 1979;3:299-308.
3. Jaszczak RJ, Coleman RE, Whitehead FR. Physical factors affecting quantitative measurements using camera-based single photon emission computed tomography (SPECT). *IEEE Trans Nucl Sci* 1981;28:69-80.
4. Kim HJ, Zeeberg BR, Fahey FH, Bice AN, Hoffman EJ, Reba RC. Three-dimensional SPECT simulations of a complex three-dimensional mathematical brain model and physical measurements of the three-dimensional physical brain phantom. *J Nucl Med* 1991;32:1923-1930.
5. Kim HJ, Zeeberg BR, Fahey FH, Hoffman EJ, Reba RC. 3D SPECT simulations of a complex 3D mathematical brain model: effects of detector response, attenuation, scatter, and statistical noise. *IEEE Trans Med Imag* 1992:in press.
6. Hoffman EJ, Cutler PD, Digby WM, Mazziotta JC. 3-D phantom to simulate cerebral blood flow and metabolic images for PET. *IEEE Trans Nucl Sci* 1990;37:616-620.
7. Chang LT. A method for attenuation correction in radionuclide computed tomography. *IEEE Trans Nucl Sci* 1978;NS-25:638-643.
8. Harris CC, Greer KL, Jaszczak RJ, et al. Tc-99m attenuation coefficients in water-filled phantoms determined with gamma cameras. *Med Phys* 1984;11:681-685.
9. Jaszczak RJ, Floyd CE, Coleman RE. Scatter compensation techniques for SPECT. *IEEE Trans Nucl Sci* 1985;32:786-793.
10. Press WH, Flannery BP, Teukolsky SA, Vetterling WT. *Numerical Recipes in C: the art of scientific computing*. Cambridge: Cambridge University Press; 1988:221-223.
11. Links JM, Loats HL, Holcomb HH, Loats SE, Stumpf MJ, Wagner HN Jr. Cortical circumferential profiling: an objective approach to cortical quantification in emission tomography [Abstract]. *J Nucl Med* 1989;30:816.
12. Budinger TF, Derenzo SE, Greenberg WL, Gullberg GT, Huesman RH. Quantitative potentials of dynamic emission computed tomography. *J Nucl Med* 1978;19:309-315.
13. Gilland DR, Jaszczak RJ, Bowsher JE, et al. Quantitative SPECT brain imaging: effects of attenuation and detector response. *IEEE NSS Conference Record* 1992:in press.
14. Zeng GL, Gullberg GT. Frequency domain implementation of the three-dimensional geometric point response correction in SPECT imaging. *IEEE NSS Conference Record* 1992:in press.
15. Chen C-T, Ouyang X, Wong WH, Hu X. Improvement of PET image reconstruction using high-resolution anatomic images. *IEEE NSS Conference Record* 1992:in press.
16. Politte DG, Snyder DL. Image reconstruction for positron-emission tomography when anatomical boundaries are known. *IEEE NSS Conference Record* 1992:in press.
17. Kim HJ, Zeeberg BR, Reba RC. Iterative reconstruction algorithm which incorporates a high resolution anatomical image: simultaneous correction for 3-D detector response, attenuation, and scatter in SPECT neuroreceptor imaging. *IEEE NSS Conference Record* 1992:in press.